electronic materials

MDPI

Article

C_{60}/CZTS Junction Combination to Improve the Efficiency of CZTS-Based Heterostructure Solar Cells: A Numerical Approach

Jobair Al Rafi [1,*], Md. Ariful Islam [2], Sayed Mahmud [2], Mitsuhiro Honda [1], Yo Ichikawa [1] and Muhammad Athar Uddin [2]

[1] Department of Physical Science and Engineering, Nagoya Institute of Technology, Nagoya 466-8555, Japan
[2] Department of Electrical and Electronic Engineering, International Islamic University Chittagong, Chittagong 4318, Bangladesh
* Correspondence: mjrafi7234@gmail.com; Tel.: +81-90-6648-5973

Abstract: This work presents a copper zinc tin sulfide (CZTS)-based solar cell structure (AI/ITO/C_{60}/CZTS/SnS/Pt) with C_{60} as a buffer layer, developed using the SCAPS-1D simulator by optimizing each parameter to calculate the output. Optimizing the parameters, the acceptor concentration and thickness were altered from 6.0×10^{15} cm^{-3} to 6.0×10^{18} cm^{-3} and 1500 nm to 3000 nm, respectively. Although, in this simulator, we can tune the value for the acceptor concentration to 6.0×10^{22}, higher doping might present an issue regarding adjustment in the physical experiment. Thus, tunable parameters need to be chosen according to the reliability of the experimental work. The defect density varied from 1.0×10^{14} cm^{-3} to 1.0×10^{17} cm^{-3} and the auger hole/electron capture coefficient was determined to be 1.0×10^{-26} cm^6 s^{-1} for the maintenance of the minorities in theoretical to quasi-proper experimental measurements. Although the temperature was intended to be kept near room temperature, this parameter was varied from 290 K to 475 K to investigate the effects of the temperature on this cell. The optimization of the proposed structure resulted in a final acceptor concentration of 6.0×10^{18} cm^{-3} and a thickness of 3000 nm at a defect density of 1.0×10^{15} cm^{-3}, which will help to satisfy the desired experimental performance. Satisfactory outcomes (V_{OC} = 1.24 V, J_{SC} = 27.03 mA/cm^2, FF = 89.96%, η = 30.18%) were found compared to the previous analysis.

Keywords: composite solar cell structure; CZTS; buffer layer; defects and minorities; SCAPS-1D

Citation: Rafi, J.A.; Islam, M.A.; Mahmud, S.; Honda, M.; Ichikawa, Y.; Athar Uddin, M. C_{60}/CZTS Junction Combination to Improve the Efficiency of CZTS-Based Heterostructure Solar Cells: A Numerical Approach. *Electron. Mater.* **2024**, *5*, 145–159. https://doi.org/10.3390/electronicmat5030010

Academic Editor: Dong Chan Lim

Received: 7 June 2024
Revised: 10 August 2024
Accepted: 14 August 2024
Published: 15 August 2024

1. Introduction

Today's world is experiencing problems for several reasons; among them are the burning of fossil fuels and the excessive energy demand. Fossil fuel combustion creates pollution by generating gases such as CO_2, NO_2, CO, SO_2, etc. [1]. Low-cost renewable energy can be used to address the environmental pollution caused by burning fossil fuels [2,3]. Photovoltaic (PV) solar cells that capture photons from the sun are a promising alternative to fossil fuels due to their significantly lower lifecycle greenhouse gas [4,5] emissions and their potential to replace fossil fuels completely. For example, covering only 0.16% of the Earth's land surface with 10% efficiency PV solar cells can satisfy the global energy demand [6]. Furthermore, solar energy contributes to energy independence, job creation, and economic growth, while also improving public health and quality of life.

A solar cell or photovoltaic (PV) cell is a device composed of semiconductor materials such as silicon, gallium arsenide, and cadmium telluride, among others, that converts sunlight directly into electricity [7,8]. More than 80% of the current photovoltaic (PV) industry is based on c-Si and p-Si wafer technologies [9,10]. When solar cells absorb sunlight, they generate free electrons and holes at positive and negative junctions. If the positive and negative junctions of the solar cells [11] are connected to direct current (DC)

electrical equipment, the current is delivered to operate the electrical equipment. A thin-film (TF) solar cell is a second-generation solar cell that is developed by coating one or more thin layers of photovoltaic material onto a substrate such as glass, plastic, or metal. Researchers are trying to introduce thin-film photovoltaic devices, an area that has greatly increased in the last decade [12]. Several materials (such as CdTe, CIS, and CIGS) have been employed by researchers to obtain low-cost and high-efficiency solar cells [13].

Thin-film PV technologies are based on direct-bandgap materials like copper indium (gallium) diselenide (CIGS), copper indium diselenide (CIS), and cadmium telluride (CdTe) and have reached the commercialization stage, with the highest reported conversion efficiency of 11% in module production [14–16]. Single-junction thin-film solar cells, which have achieved high efficiency and show excellent performance, utilize GaAs [17], CdTe, or $Cu(In,Ga)Se_2$ (CIGS) [18] as the absorber. Due to the toxicity of Cd and Se and availability issues for In and Te, the production of PV devices based on this absorber layer is limited [19]. In the case of GaAs and CdTe, the toxicity concerns associated with the use of arsenic and cadmium, respectively, may limit their widespread application [20,21]. For CIGS, the use of indium reduces its potential to reach the terawatt scale due to the limited number of economic reserves and the high material costs resulting from the large demand from the display industry [22]. Quaternary semiconductors with a kestrite mineral structure are promising candidates to satisfy the requirements of low-cost and eco-friendly thin-film solar cells [23]. Copper zinc tin sulfide (CZTS) has attracted the attention of many researchers as it is a promising compound in the sense that it fulfills two essential conditions. Indeed, it is composed of eco-friendly and low-cost elements [24]. A recent research paper explored the use of a non-toxic Zn (O, S) buffer layer in CZTS solar cells as an alternative to CdS, highlighting its tunable optical bandgap and potential for improved efficiency. However, the challenges in accurately modeling defects and traps in the layers/interfaces and the need for further optimization of the Zn (O, S)/CZTS solar cell structure for enhanced performance represent obstacles [25]. Another finding was highlighted by Siham et al., demonstrating the exceptional performance of MoOx and CuI as HTLs, surpassing SnS by a significant margin. Specifically, MoOx and CuI demonstrate remarkable power conversion efficiency of 23.73% [26]. The incorporation of SnS as an ETL with CZTS has been demonstrated in a previous study where the utilization of SnS_2 as the ETL material in conjunction with CZTS as the absorber layer material yielded the maximum efficiency of 21.89%, an open-circuit voltage (V_{OC}) of 0.97 V, a short-circuit current density (J_{SC}) of 26.53 mA/cm^2, and a fill factor (FF) of 84.86% [27]. Another study focused on enhancing a Cu_2ZnSnS_4 (CZTS)-based solar cell's performance by incorporating ultrathin Zr and W interlayers at the SnO_2:F/CZTS interface, aiming to improve the ohmic properties of the back contacts and the overall cell efficiency [28].

The copper zinc tin sulfide (CZTS) mineral is found in nature [29]. The copper zinc tin chalcogenide is a quaternary semiconductor of group I-II-IV-VI that was first elaborated in 1966, and, afterward, its photovoltaic effect was confirmed in 1988 [24,30]. There has been extensive investigation into the use of other materials to replace the harmful CdS buffer layer in CZTS-based solar cells [31]. CZTS is classified into two crystallographic types: stannite and kieserite. The two structures are similar except for the placement of the Cu and Zn atoms. However, the CZTS material frequently arises in the kieserite phase because it is thermodynamically more stable than stannite. The scientific community has become more interested in non-toxic, low-cost, and readily available absorber materials. CZTS-based materials are p-type semiconductors with a hole density of around 10^{16} cm^{-3}, which is characteristic of CIGS in high-efficiency CIGS solar cells [32]. Thus, it can be stated that a Cu_2ZnSnS_4 (CZTS) quaternary semiconductor is a good choice for solar absorber materials. The components of CZTS are abundant in the Earth's crust (Cu: 50 ppm, Zn: 75 ppm, Sn: 2.2 ppm, S: 260 ppm) and have exceedingly low toxicity. Moreover, other properties of CZTS, such as the high absorption coefficient of over 10^4 cm^{-1} and the direct bandgap value of about 1.4–1.5 eV, make these solar cells attractive candidates [33]. The highest laboratory-level CZTS solar cell efficiency is 8.4% [34], while the theoretical

conversion efficiency of 18.05% for CZTS/CdS solar cells was reported in 2017 [35]. CZTS-based materials are highly suitable for use as absorbers. Firstly, they possess a Shockley–Queisser limit (SQL) of at least 30.9% (for a bandgap of 1.0 eV) [36]. This minimum is close to the SQL maximum of 33.7% for a single-junction solar cell with a bandgap of 1.34 eV [37,38].

Fullerene-C_{60}, also known as Buckminsterfullerene, stands out for its unique structure, which simulates a hollow ball formed of carbon atoms; C_{60} has been utilized as a hole blocking layer (HBL) and an electron injection layer (EIL) to enhance the performance [39]. It is adept in transporting electrons and is compatible with the materials used in solar panels. Electron transport layers (ETL) promote charge extraction, minimize recombination losses, and increase the overall device efficiency. The efficient movement of electrons from the CZTS layer to the electrode reduces energy waste and improves the total solar panel performance. In some previous studies, researchers have introduced SnS as a potential BSF to achieve high power conversion efficiency in solar cells [40–42]. Surface recombination at the back contact is a significant obstacle in these devices. To address this issue, this work introduces back-surface field (BSF) layers to minimize back-surface recombination. Tin sulfide (SnS) is employed as the BSF material in this context.

In this work, a heterostructure is proposed via the junction (n/p) created with fullerene (C_{60}) and CZTS. The aim is to use this CZTS-based heterostructure with fullerene to improve cell efficiency, along with the other outputs. In this structure, optimization is implemented, showing comparatively better outcomes than the previous CZTS-based heterostructure model [43]. This theoretical study is conducted using a computer-based numerical simulation. The literature and comparative studies are discussed with regard to similar previous works for a better understanding of the improvements in this relevant field. In a physical experiment, a structure with the same parameters might show poorer outcomes than in a simulation regarding actual defects and focusing on materials with individual minorities. A clear difference can be seen through the comparison of similar works.

2. Device Modeling and Simulation Parameters

The suggested structure, Al/ITO/C_{60}/CZTS/SnS/Pt, was analyzed numerically using the SCAPS-1D simulator. SCAPS-1D is a one-dimensional simulator that uses steady-state solutions to three essential equations for semiconductor devices: Poisson's equation, the continuity equation for free holes, and the continuity equation for free electrons [44,45]. To utilize this computer-based simulator, the electrical and optical properties of each designated layer are used as simulation input parameters. It enables the simulation of the physical and electrical structures of heterojunctions, homojunctions, multifunction's, and even Schottky barriers. This simulator can regulate each layer's specific input settings.

The Poisson equation:

$$div(\varepsilon \nabla \Psi) = -\rho \tag{1}$$

The continuity equation for free electrons:

$$\frac{\partial n}{\partial t} = \frac{1}{q} di\vec{v} j_n + G_n - R_n \tag{2}$$

The continuity equation for free holes:

$$\frac{\partial p}{\partial t} = -\frac{1}{q} di\vec{v} j_p + G_p - R_p \tag{3}$$

where ε = Dielectric permittivity; Ψ = Electrostatic potential field; n, p = Electron and hole concentrations; G_n, G_p = Generation rate of electrons and holes; R_n, R_p = Recombination rate of electrons and holes; j_n, j_p = Current densities of electrons and holes.

Figure 1 shows the planar device structure of the designated final solar cell. The substrate-type device structure is used here, and the construction of the device's structure is mostly affected by the technological feasibility and success in CZTS-based solar cell applications.

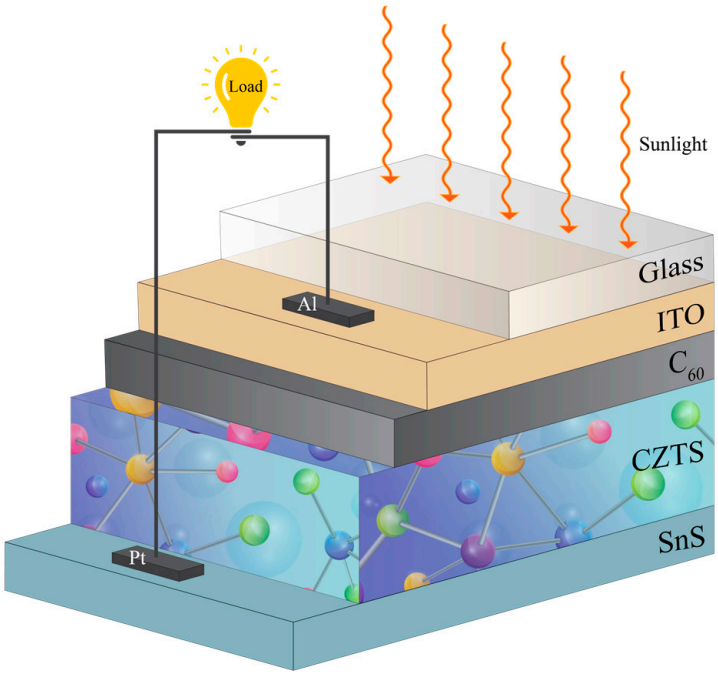

Figure 1. Structural model of the proposed solar cell device (Al/ITO/C_{60}/CZTS/SnS/Pt).

Table 1 shows the input parameters of each layer used to create the proposed heterostructure. Here, two parameters (the thickness and acceptor concentration) of the absorber, CZTS, are tuned from 1500 nm to 3000 nm and 6.0×10^{15} cm^{-3} to 6.0×10^{18} cm^{-3}, respectively.

Table 1. Parameters used to simulate the heterostructure cell ITO/C_{60}/CZTS/SnS.

Parameter	ITO [46]	C_{60} [47]	CZTS [43]	SnS [46]
Thickness (nm)	50	20	1500–3000	100
Bandgap E_g (eV)	3.5	1.7	1.5	1.6
Electron affinity, χ (eV)	4.6	4.5	4.58	4.1
Dielectric permittivity	8.9	6.0	9.5	13.0
CB effective density of states (cm^{-3})	2.2×10^{18}	1.0×10^{19}	1.91×10^{18}	2.18×10^{18}
VB effective density of states (cm^{-3})	1.8×10^{19}	1.0×10^{19}	2.58×10^{18}	4.46×10^{18}
Electron thermal velocity (cm s^{-1})	1.0×10^{7}	1.0×10^{7}	1.0×10^{7}	1.0×10^{7}
Hole thermal velocity (cm s^{-1})	1.0×10^{7}	1.0×10^{7}	1.0×10^{7}	1.0×10^{7}
Electron mobility, μ_n (cm^2 V^{-1} s^{-1})	10	50	50	15
Hole mobility, μ_p (cm^2 V^{-1} s^{-1})	10	50	10	100
Donor concentration, N_D (cm^{-3})	1.0×10^{19}	1.0×10^{18}	0.0	0.0
Acceptor concentration, N_A (cm^{-3})	0.0	0.0	6.0×10^{15}–6.0×10^{18}	1.0×10^{19}

Table 2 describes the characteristics of the front and back contacts employed in this study. The value of the surface recombination velocity is utilized alternately for electrons and holes, as described in prior published work [46,48–50]. Individual contact has been assigned a work function.

Table 2. Front and back contact parameters.

Parameter	Front Contact Electrical Properties	Back Contact Electrical Properties
	[Al]	[Pt]
Surface recombination velocity of electrons (cm s^{-1})	1.0×10^{7}	1.0×10^{5}
Surface recombination velocity of holes (cm s^{-1})	1.0×10^{5}	1.0×10^{7}
Work function (eV)	4.26	5.65

Table 3 displays the interface defect parameters for three interfaces constructed using (i) n-type/n-type, (ii) n-type/p-type, and (iii) p-type/p-type structures, with a Gaussian energy distribution utilized in the junction (n/p) established in this structure.

Table 3. Interface defect parameters.

Parameter	ITO/C_{60}	C_{60}/CZTS	CZTS/SnS
Defect type	Neutral	Neutral	Neutral
Capture cross-section of electrons (cm^2)	1.0×10^{-19}	1.0×10^{-19}	1.0×10^{-19}
Capture cross-section of holes (cm^2)	1.0×10^{-19}	1.0×10^{-19}	1.0×10^{-19}
Energetic distribution	Single	Gaussian	Single
Total defect density (cm^{-2})	1.0×10^{10}	1.0×10^{10}	1.0×10^{10}

Table 4 shows the defect parameters for specific semiconductor layers, which are calculated as a combination of minority and crystal defects. The defects range from 1.0×10^{14} to 1.0×10^{17} cm^{-3} for a reasonable conclusion with a comparably superior outcome. We use a single energetic distribution and the capture cross-sections of electrons and holes are kept at 1.0×10^{-15} cm^2 for each semiconductor layer. The Auger hole/electron capture coefficient, which has been set at 1.0×10^{-26} cm^6 s^{-1}, is crucial in maintaining the minority carrier concentrations in theoretical models. This value ensures consistency when comparing theoretical predictions to quasi-experimental measurements, thereby enhancing the reliability and accuracy of the experimental validation. To physically replicate a heterostructure cell, a composite composed of appropriate semiconductors is necessary. Semiconductors frequently require minority and crystal defects to create a junction.

Table 4. Individual layers' defect parameters.

Parameter	At Each Layer (ITO, C_{60}, CZTS, SnS)
Defect type	Neutral
Capture cross-section of electrons (cm^2)	1.0×10^{-15}
Capture cross-section of holes (cm^2)	1.0×10^{-15}
Energetic distribution	Single
Reference for defect energy level Et	Above EV (SCAPS < 2.7)
Total density (cm^{-3}): uniform	1.0×10^{14}–1.0×10^{17}
Auger hole/electron capture coefficient (cm^6 s^{-1})	1.0×10^{-26}

3. Simulation Results and Discussion

Structure—Al/ITO/C_{60}/CZTS/SnS/Pt

3.1. Band Diagram

Figure 2 shows the band diagram of the introduced heterostructure to illustrate its band bending and quasi-Fermi levels. Here, the two solid lines in blue and red indicate the valance band and conduction band, respectively. Fn and Fp indicate the electron–hole pair generation in this device.

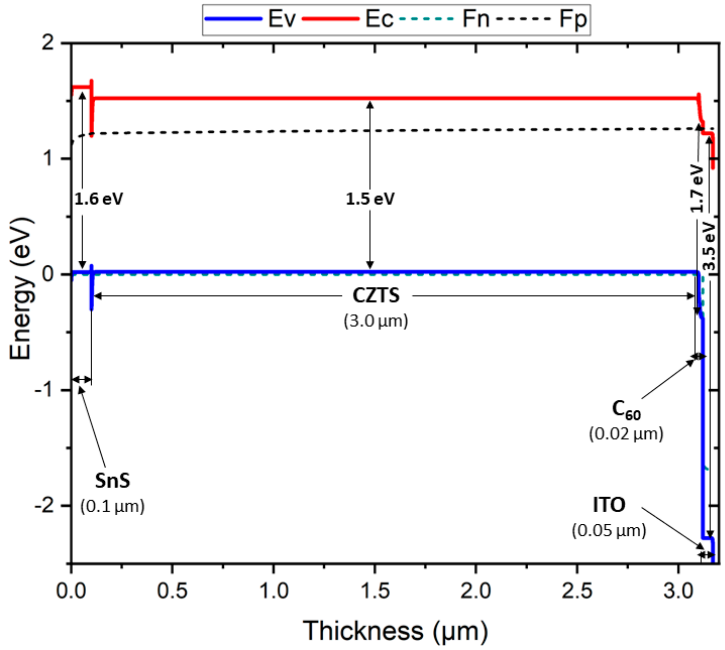

Figure 2. Energy band diagram of the proposed heterostructure cell—ITO/C_{60}/CZTS/SnS.

3.2. Effect of Absorber Layer Thickness and Acceptor Concentration on PV Performance

The principal design specifications that affect solar cell activities are the absorber concentration and absorber layer thickness. The acceptor concentration (N_A) and absorber layer thickness must be adjusted to achieve optimal solar cell performance. To assess the cell performance, the absorber layer thickness and acceptor concentration were adjusted in 4 steps, from 1.5 µm to 3.0 µm and from 6×10^{15} cm^{-3} to 6×10^{18} cm^{-3}, respectively. The dual effects of the absorber layer thickness and concentration on the PV parameters V_{OC}, J_{SC}, FF, and %η in the structure under assessment, Al/ITO/C_{60}/CZTS/SnS/Pt, are presented in Figure 3. The figure indicates that the absorber layer concentration is a key component of the cell performance, and adjusting the absorber layer and CZTS acceptor concentration can alter the %η. Figure 3a–d show the open-circuit voltage, short-circuit current, fill factor, and efficiency.

Figure 3a shows that although the open-circuit voltage fluctuates in response to modifications in the acceptor concentration, it is mostly unaffected by changes in the absorber thickness. Additionally, the concentration of 6×10^{16} is followed by an increased range of open-circuit voltages. This can be attributed to the drop in the reverse saturation current that occurs with increased carrier concentrations, which increases the V_{OC}. Figure 3b illustrates how the short-circuit current decreases with the acceptor concentration but slightly increases with the thickness. The increase in the short-circuit current observed with the increasing CZTS thickness and decreasing acceptor concentration can be attributed to the enhanced absorption of longer-wavelength photons within this layer. In Figure 3c, the fill factor exhibits behavior similar to that of the open-circuit voltage, although it is not assigned the same value at every thickness. Additionally, the key output efficiency increases at the concentrations of 6×10^{17} to 6×10^{18} and the thickness increases significantly. The fill factor (FF) shows a slight drop when the CZTS layer thickness grows, and the acceptor concentration is reduced. This is mostly due to an increase in the device's series resistance. Although it is difficult to sustain high doping for every material, CZTS exhibits superior efficiency at higher doping levels. However, this value is still limited since the highest value that we can obtain is 10^{22}.

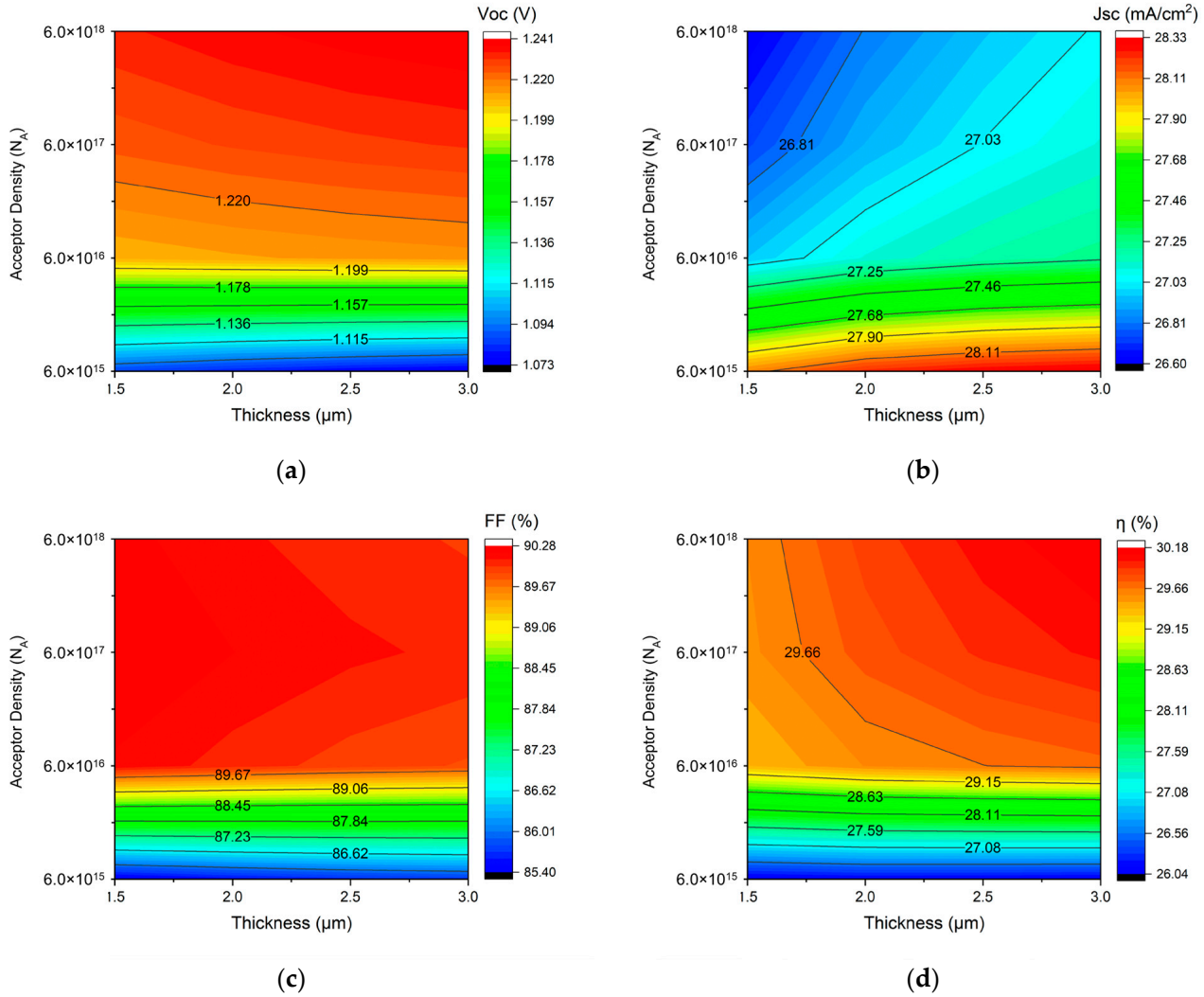

Figure 3. Simultaneous implications of acceptor concentration and thickness of absorber layer on performance ((**a**) V_{OC}, (**b**) J_{SC}, (**c**) FF, and (**d**) %η) of CZTS-based solar cell.

In summary, every output displays the maximum range of values at the highest thickness. Furthermore, three outputs, excluding the short-circuit current, show the maximum values following the concentration of 6×10^{17} cm^{-3}. Although the outcomes of this study are obtained at lower concentrations compared to previous research, 6×10^{18} is recommended as the optimal value for comparable performance.

Table 5 provides an overview of the optimal input conditions and final outcomes obtained from this proposed structure. These output parameters outperform those of earlier CZTS-based work, although the input values were kept consistent with past studies.

Table 5. Optimum inputs (thickness and acceptor concentration) and outputs at optimum conditions.

Optimum Input Conditions		Output Parameters at Optimized Input Conditions			
W (μm)	**N_A (cm^{-3})**	**V_{OC} (V)**	**J_{SC} (mA/cm^2)**	**FF (%)**	**η (%)**
3.0	6×10^{18}	1.2405	27.039539	89.96	30.18

Figure 4 shows the normalized values of all outputs (V_{OC}, J_{SC}, FF, and %η), plotted against the acceptor concentration in Figure 4a and the thickness in Figure 4b. The normalized values are estimated based on the highest values of the individual outputs. The efficiency (%η) was obtained at the maximum while keeping the other outputs (V_{OC}, J_{SC},

and FF) satisfactory. The optimal input factors (thickness = 3 μm and $N_A = 6 \times 10^{18}$ cm^{-3}) result in a normalized value of %η = 1.0 and other normalized outcomes of 0.90 or higher.

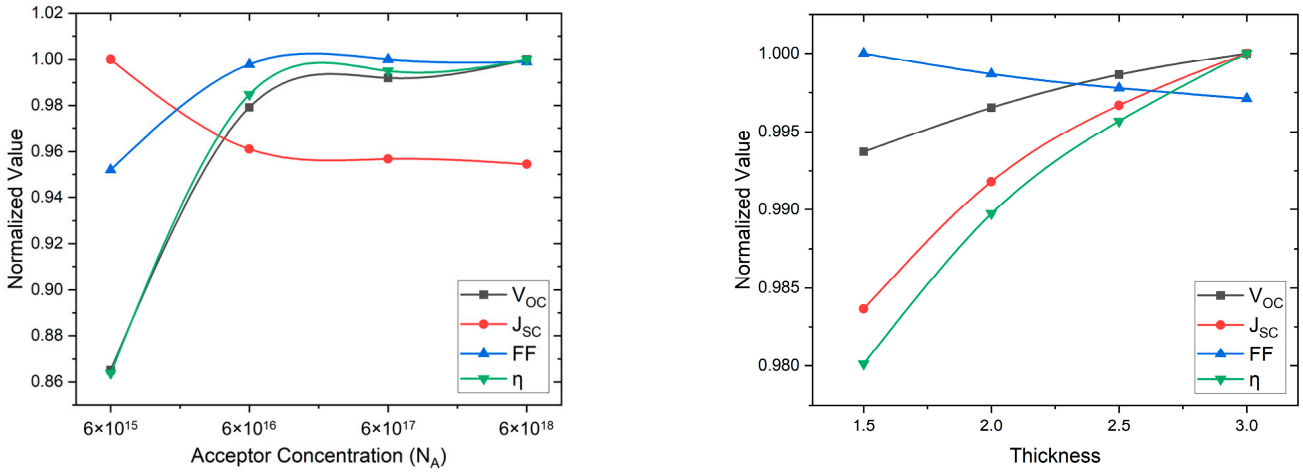

(**a**) (**b**)

Figure 4. Normalized values of solar cell output parameters as a function of (**a**) acceptor concentration and (**b**) thickness.

3.2.1. Effect of Defect Density

Imperfections in a realistic active material are caused by dislocations and grain boundaries. These flaws act as carrier recombination centers, reducing the carrier lifetime and mobility. Figure 5 displays the combined effect of the defect density and absorber layer thickness on the solar cell performance to evaluate the device's performance. The influence of the defect density between 1×10^{14} cm^{-3} and 1×10^{17} cm^{-3} and the thickness between 1.5 and 3.0 μm is explored in this study. Figure 5 illustrates how V_{OC} fluctuates slightly with the thickness at a defect level below 1×10^{15} cm^{-3}, where a regular variation in the defect density is noted. When the acceptor concentration is lower, V_{OC} indicates its highest output; however, as the thickness increases, it also increases the value of V_{OC}. The reducing behavior of J_{SC} is quite similar to that of V_{OC}. However, J_{SC} reaches higher values when the thickness drops between 2.5 μm and 3.0 μm, and this value is affected by an increase in defects. Additionally, FF and η mostly follow the J_{SC} and V_{OC} outputs. The efficiency is roughly the same as the short-circuit current, although the fill factor is larger at moderate thickness values. When the defect density in the absorber layer surpasses 1×10^{16} cm^{-3}, the cell performance deteriorates significantly. This decline is likely due to an increase in trap-assisted carrier recombination, as illustrated in the figure. The power conversion efficiency (PCE) decreases from 31.21% to 19.31%. According to this research, Shockley–Read–Hall (SRH) recombination significantly affects the loss of cell efficiency when the absorber layer contains many defects. This process involves carrier recombination in semiconductors through defect states within the bandgap. Such defects, often resulting from impurities or structural imperfections, can capture and recombine charge carriers (electrons and holes), thus lowering the overall efficiency of the semiconductor device. After combining these, we discovered that this absorber layer, with a greater thickness, can address the issue of lower outcomes, as shown at the above concentration. This can therefore continue to be increased because this range of thicknesses does not affect the experimental work.

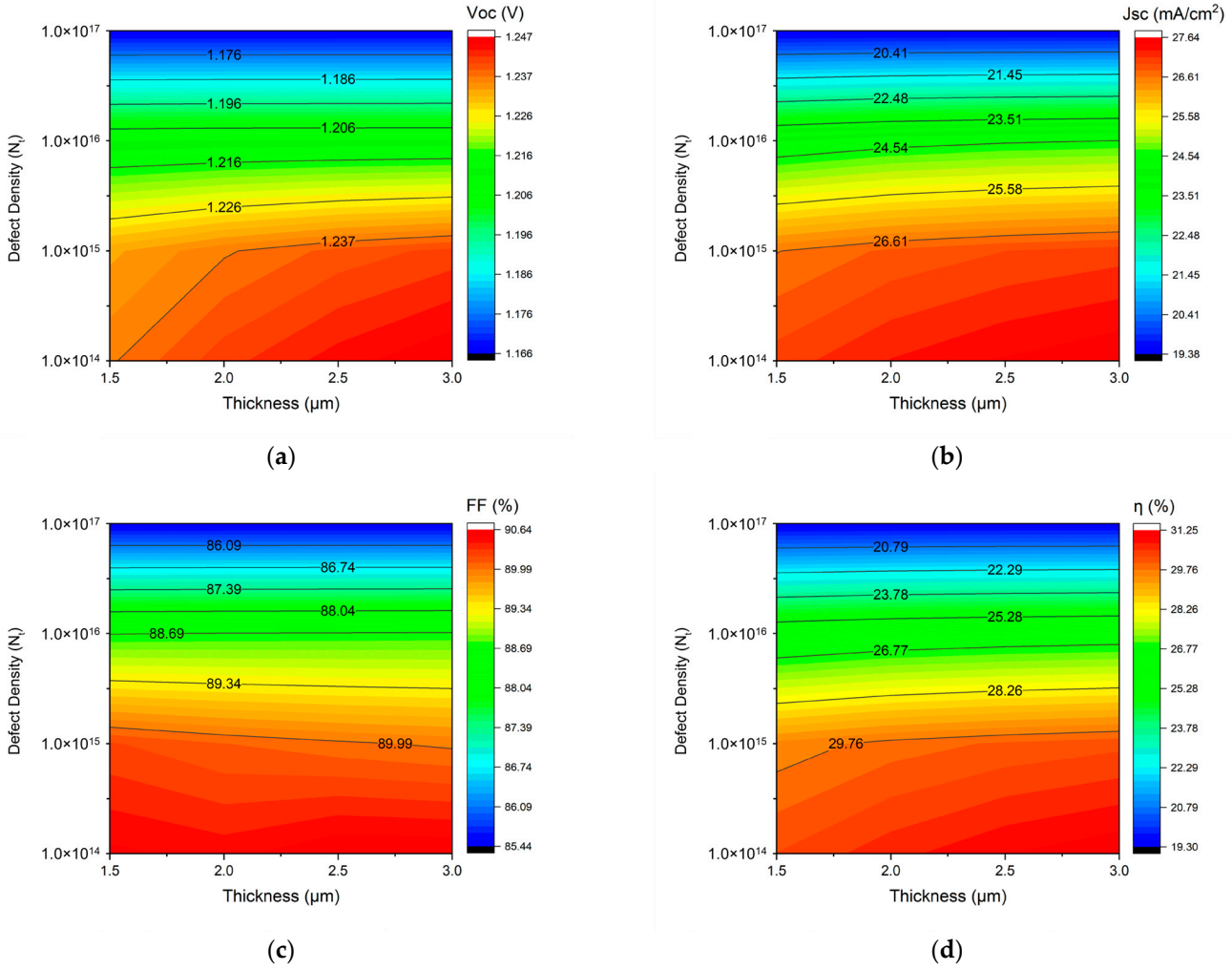

Figure 5. Impact of defect density and absorber layer thickness on PV performance parameters ((**a**) V_{OC}, (**b**) J_{SC}, (**c**) FF, and (**d**) %η) of CZTS-based solar cell.

3.2.2. Effect of Series and Shunt Resistance

Series resistance (R_S) and shunt resistance (R_{Sh}) have a substantial impact on the solar cell efficiency, primarily due to interlayer connections, metal contacts, and manufacturing defects within the cell structure. Figure 6 illustrates the variation in R_S from 0 to 6 Ω-cm^2, while keeping the shunt resistance constant at 1 × 10^5 Ω-cm^2 for the Al/ITO/C_{60}/CZTS/SnS/Pt structure. During the R_S variation, the power conversion efficiency (PCE) of the proposed device structure decreased. Specifically, as shown in Figure 6a, the PCE dropped from 29.5% to 26% as R_S increased. Additionally, the fill factor (FF) value also decreased with the increase in R_S. The J_{SC} and V_{OC} performance remained nearly constant with the increase in R_S, indicating that the R_S variation does not significantly impact these parameters for the studied device configurations. R_S comprises the resistances between various terminals, such as the absorber, the ETL, the HTL, and the front and back contacts of the cell, which do not affect the current up to a certain threshold.

Series resistance (R_S) originates from internal resistances, interface barriers, charge-collecting interlayers, and metal electrodes. In contrast, shunt resistance (R_{Sh}) is caused by leakage pathways like pinholes in the photoactive layer and recombination losses. The effect of the V_{OC}, J_{SC}, FF, and PCE values with R_{Sh} variation is visually represented in Figure 6b, with R_{Sh} ranging from 10^1 to 10^7 Ω-cm^2. The V_{OC}, J_{SC}, FF, and PCE values displayed a similar trend with increasing shunt resistance (R_{Sh}). All performance parameters rose rapidly from 10^1 Ω-cm^2 to 10^3 Ω-cm^2 and then stabilized as R_{Sh} continued to increase.

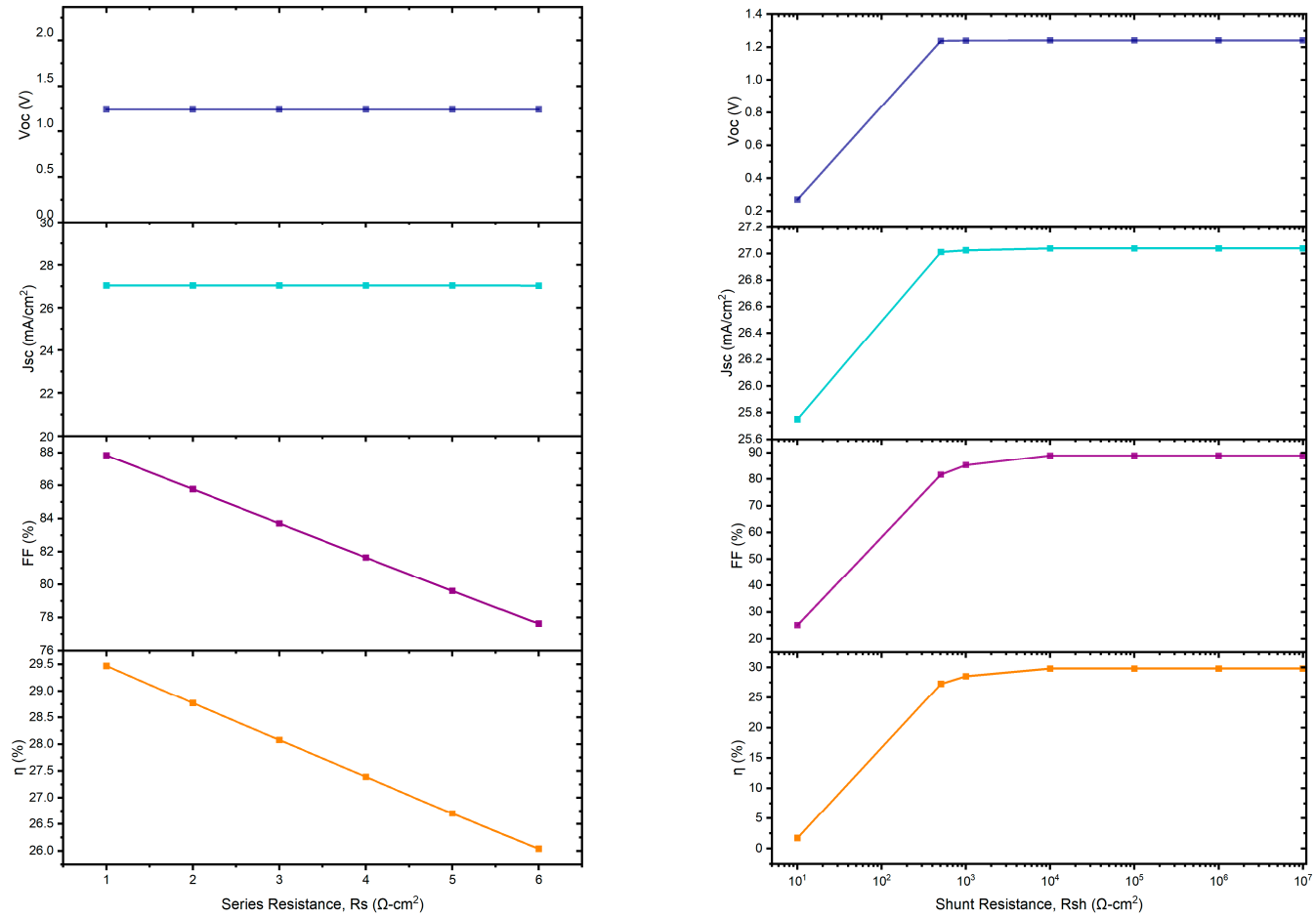

Figure 6. Impact of (**a**) series and (**b**) shunt resistance on PV performance (V_{OC}, J_{SC}, FF, and PCE).

3.2.3. Effect of Temperature

A thorough understanding of the solar cell's performance at elevated operating temperatures is crucial in assessing its stability. High temperatures typically cause layer distortion, resulting in performance instability in most solar cell designs. To investigate the effect of the temperature on the solar cell efficiency, the temperature range was adjusted from 298 K to 480 K. Figure 7a,c,d demonstrate that with rising temperatures, the power conversion efficiency (PCE), fill factor (FF), and open-circuit voltage (V_{OC}) decrease across the solar cell configurations. However, in Figure 7b, the short-circuit current (J_{SC}) exhibits a slight upward variation, increasing marginally from 27 to 27.4 mA/cm^2, contrasting with the more pronounced decreases observed in the other parameters. Nevertheless, the open-circuit voltage (V_{OC}) decreased for the optimal device configurations as the temperature increased. This was due to the inverse relationship between V_{OC} and the reverse saturation current density, J_0. As the temperature rises, J_0 increases, as shown in Equation (4), which illustrates the relationship between V_{OC} and J_0.

$$V_{OC} = \frac{Ak_BT_1}{q}\left[ln\left(1 + \frac{J_{SC}}{J_0}\right)\right] \quad (4)$$

In this equation, $\frac{k_BT_1}{q}$ represents the thermal voltage, where k_B is the Boltzmann constant, q is the electron charge, and A denotes the ideality factor.

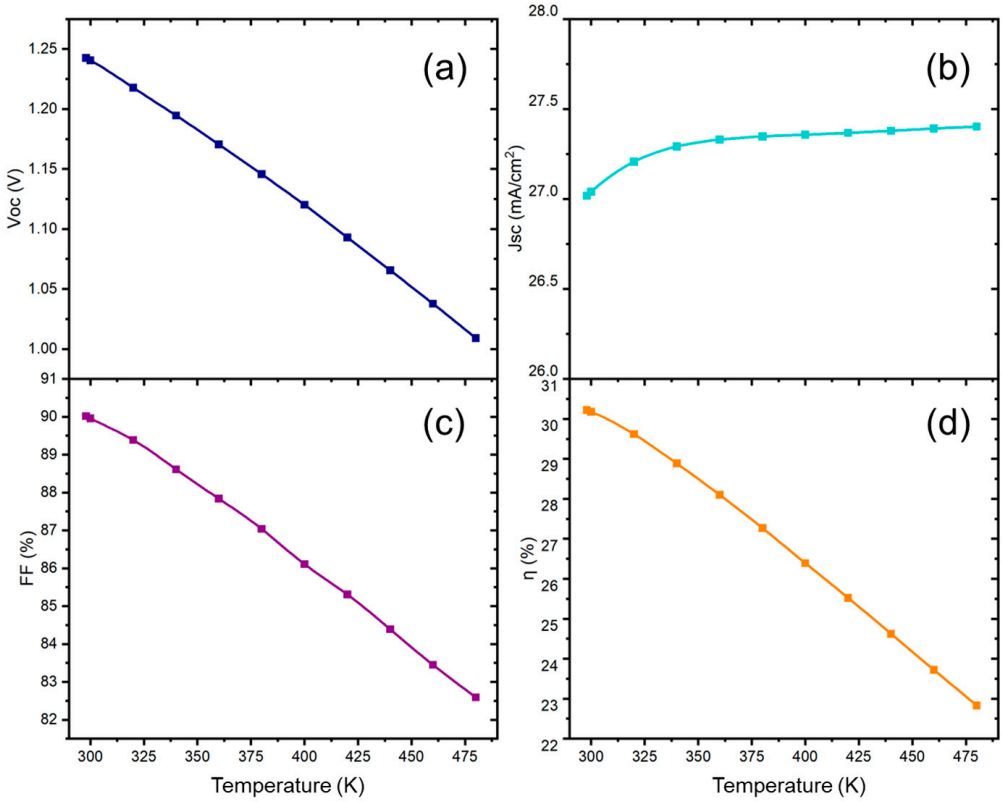

Figure 7. Effect of temperature on solar cell performance parameters: (**a**) open-circuit voltage (V_{OC}), (**b**) short-circuit current (J_{SC}), (**c**) fill factor (FF), and (**d**) efficiency (η%).

Additionally, as the temperature of the model increases, the material defects are exacerbated, leading to a further decrease in V_{OC}. Figure 7b demonstrates that the current increases slightly due to the reduction in the bandgap with the rising temperature. However, this increase is minimal, and the change in current remains nearly constant as the temperature continues to rise.

3.2.4. Effect of Capacitance and Mott–Schottky

Figure 8a,b illustrates the capacitance per unit area (C) and the Mott–Schottky (M–S) plot as functions of the bias voltage (V), respectively. From these C–V measurements, the built-in voltage (V_{bi}) and charge carrier density (N_d) can be derived using the established M–S analysis method. This technique is traditionally applied to semiconductor devices with fixed depletion layers and space charge regions, such as those with p–n junctions or semiconductor/metal interfaces. Equation (5) provides the value of the junction capacitance per unit area (C).

$$\frac{1}{C^2} = \frac{2\varepsilon_0\varepsilon_r}{qN_d}(V_{bi} - V) \tag{5}$$

Here, ε_0 represents the vacuum permittivity, ε_r denotes the donor's dielectric constant, and V stands for the applied voltage (Figure 8b).

The donor density (N_d) is derived from the slope of the linear segment, while the built-in voltage V_{bi} is determined by extrapolating the linear portion to intersect the voltage axis. This device exhibits voltage-independent capacitance ranging from −0.4 V to 0.5 V, with an exponential increase observed beyond 0.5 V (Figure 8a).

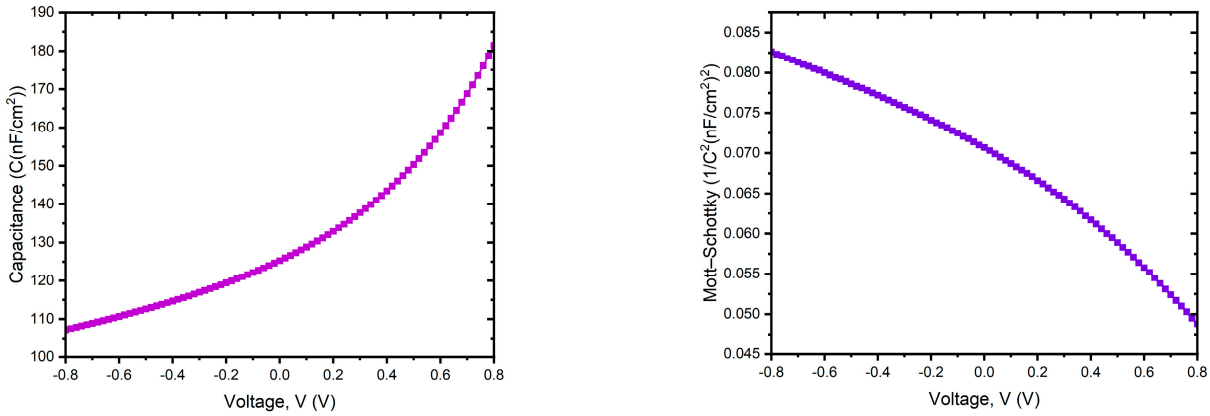

(**a**) (**b**)

Figure 8. (**a**) Capacitance (C) and (**b**) Mott–Schottky ($1/C^2$) plot for the proposed structure.

3.2.5. Effect of Generation and Recombination Rate

Figure 9a,b depicts the rates of carrier generation and recombination, respectively. During carrier generation, electron–hole pairs are formed as electrons are excited from the valence band to the conduction band, leaving behind holes in the valence band. This generation process results from the emission of electrons and holes.

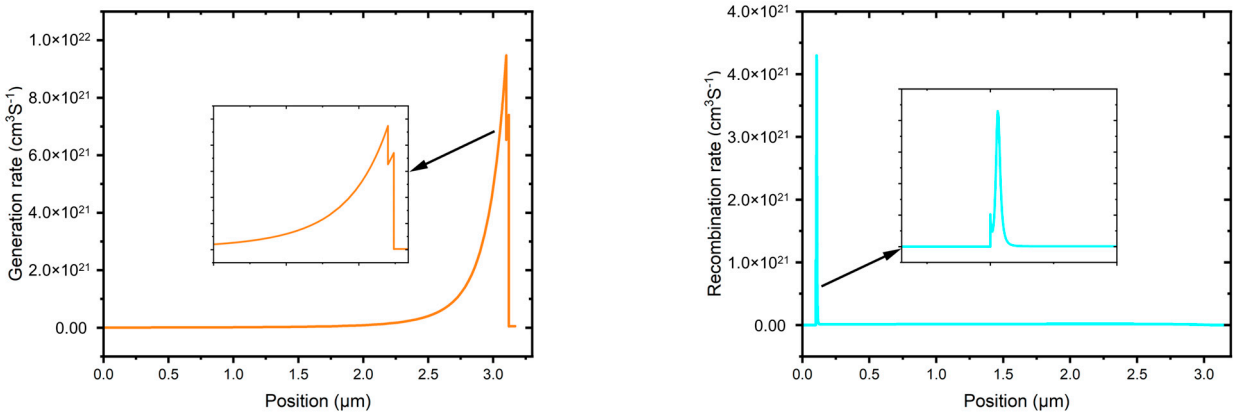

(**a**) (**b**)

Figure 9. (**a**) Generation rate and (**b**) recombination rate for the proposed structure.

Recombination is the reverse of generation, where electrons and holes from the conduction band pair up and are annihilated. The recombination rate in a solar cell is influenced by the charge carrier's lifespan and density. Initially, electron–hole recombination is reduced due to defect states within the absorber layer. These defect states create energy levels that affect the electron–hole recombination profile within the solar cell structure. Consequently, the recombination rate distribution is non-uniform, as indicated in Figure 9b, due to imperfections and grain boundaries.

3.2.6. J–V and QE Characteristics

Figure 10a shows the J–V characteristic changing pattern of the proposed structure. The current density exhibits a high value of 27 mA/cm^2. In addition, the voltage is higher than 1.0 V, which indicates that the structure exhibits better performance.

Figure 10b illustrates the quantum efficiency (QE) curve across different wavelengths. The proposed configuration achieved a peak QE close to 100% at a wavelength of 300 nm. However, recombination, which prevents charge carriers from entering the external circuit, generally reduces the QE of most solar cells. The QE is influenced by the same factors that

affect the collection probability. For example, modifications to the front surface can impact carriers generated near the surface. Additionally, highly doped front surface layers can lead to free carrier absorption, which decreases the QE at longer wavelengths.

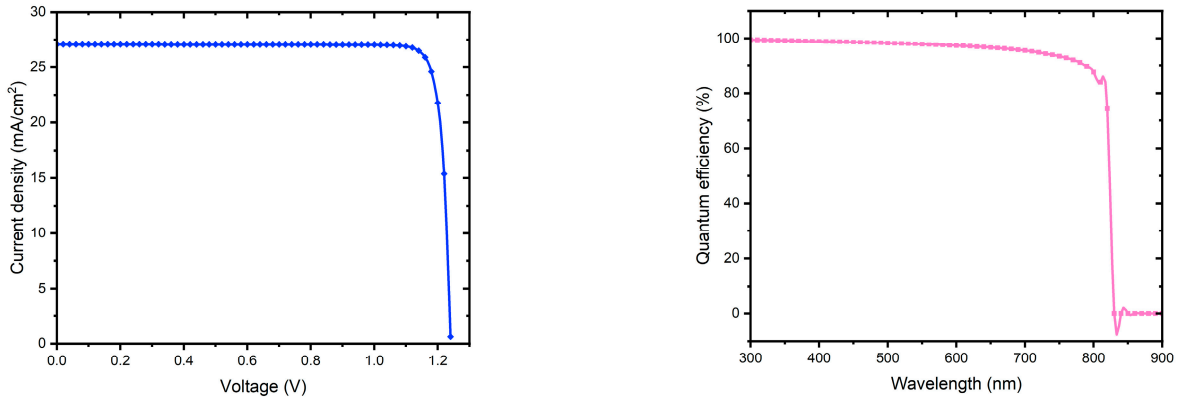

(**a**) (**b**)

Figure 10. (**a**) J–V characteristics and (**b**) quantum efficiency (QE) plot of the proposed structure.

4. Conclusions

This numerical work has been performed using several input parameters that lead to unique characteristics for different materials. From these parameters—the thickness, bandgap, electron affinity, dielectric permittivity, CB/VB effective density of states, electron–hole thermal velocity, electron–hole mobility, and acceptor/donor concentration—we have optimized the thickness and acceptor concentration for the absorber layer. Additionally, in this work, we sought to examine how the proposed structure behaved with defects and minorities. Thus, after optimizing two input parameters, the thickness and acceptor concentration, we tuned the layer defects and set the appropriate band-to-band recombination (auger hole–electron capture coefficient) and three interface defects. Finally, the calculated results (open-circuit voltage, short-circuit current, fill factor, and efficiency) for the optimized structure were obtained as 1.2405 V, 27.039539 mA/cm^2, 89.96%, and 30.18%, respectively, which are comparatively better than those obtained in preceding studies. However, in this study, the optimized input parameters were maintained according to previous studies. It is hoped that the accuracy and reliability of our method will inspire researchers to conduct further experimental work.

Author Contributions: Conceptualization, J.A.R. and M.A.I.; methodology, J.A.R. and M.A.I.; software, J.A.R. and M.A.I.; validation, J.A.R., M.A.I., M.H. and Y.I.; formal analysis, J.A.R., M.A.I., S.M., M.H., Y.I. and M.A.U.; investigation, J.A.R., M.A.I., S.M., M.H., Y.I. and M.A.U.; resources, J.A.R. and M.A.I.; data curation, J.A.R. and M.A.I.; writing—original draft preparation, J.A.R., M.A.I. and S.M.; writing—review and editing, J.A.R., M.A.I. and M.H.; visualization, J.A.R., M.A.I., S.M., M.H., Y.I. and M.A.U.; supervision, M.H., Y.I. and M.A.U. All authors have read and agreed to the published version of the manuscript.

Funding: This research received no external funding.

Data Availability Statement: Data are contained within the article.

Conflicts of Interest: The authors declare no conflicts of interest.

References

1. Suryawanshi, M.P.; Agawane, G.L.; Bhosale, S.M.; Shin, S.W.; Patil, P.S.; Kim, J.H.; Moholkar, A.V. CZTS Based Thin Film Solar Cells: A Status Review. *Mater. Technol.* **2013**, *28*, 98–109. [CrossRef]
2. Vallisree, S.; Thangavel, R.; Lenka, T.R. Theoretical Investigations on Enhancement of Photovoltaic Efficiency of Nanostructured CZTS/ZnS/ZnO Based Solar Cell Device. *J. Mater. Sci. Mater. Electron.* **2018**, *29*, 7262–7272. [CrossRef]

3. Reshak, A.H.; Nouneh, K.; Kityk, I.V.; Bila, J.; Auluck, S.; Kamarudin, H.; Sekkat, Z. Structural, Electronic and Optical Properties in Earth- Abundant Photovoltaic Absorber of Cu_2ZnSnS_4 and $Cu_2ZnSnSe_4$ from DFT Calculations. *Int. J. Electrochem. Sci.* **2014**, *9*, 955–974. [CrossRef]
4. Mekhilef, S.; Saidur, R.; Safari, A. A Review on Solar Energy Use in Industries. *Renew. Sustain. Energy Rev.* **2011**, *15*, 1777–1790. [CrossRef]
5. Hosenuzzaman, M.; Rahim, N.A.; Selvaraj, J.; Hasanuzzaman, M.; Malek, A.B.M.A.; Nahar, A. Global Prospects, Progress, Policies, and Environmental Impact of Solar Photovoltaic Power Generation. *Renew. Sustain. Energy Rev.* **2015**, *41*, 284–297. [CrossRef]
6. Graetzel, M.; Janssen, R.A.J.; Mitzi, D.B.; Sargent, E.H. Materials Interface Engineering for Solution-Processed Photovoltaics. *Nature* **2012**, *488*, 304–312. [CrossRef] [PubMed]
7. Gupta, S. An Evolution Review in Solar Photovoltaic Materials. *J. Commun. Technol. Electron. Comput. Sci.* **2018**, *20*, 7–15.
8. Jaiswal, D.; Mittal, M.; Mittal, V. A Review on Solar PV Cell and Its Evolution. In *Proceedings of the Latest Trends in Renewable Energy Technologies*; Vadhera, S., Umre, B.S., Kalam, A., Eds.; Springer: Singapore, 2021; pp. 303–313.
9. Mitzi, D.B.; Gunawan, O.; Todorov, T.K.; Wang, K.; Guha, S. The Path towards a High-Performance Solution-Processed Kesterite Solar Cell. *Sol. Energy Mater. Sol. Cells* **2011**, *95*, 1421–1436. [CrossRef]
10. ur Rehman, A.; Iqbal, M.Z.; Bhopal, M.F.; Khan, M.F.; Hussain, F.; Iqbal, J.; Khan, M.; Lee, S.H. Development and Prospects of Surface Passivation Schemes for High-Efficiency c-Si Solar Cells. *Sol. Energy* **2018**, *166*, 90–97. [CrossRef]
11. Irvine, S. Solar Cells and Photovoltaics. In *Springer Handbook of Electronic and Photonic Materials*; Kasap, S., Capper, P., Eds.; Springer International Publishing: Cham, Switzerland, 2017; pp. 1097–1109. ISBN 978-3-319-48933-9.
12. Gunaicha, P.P.; Gangam, S.; Roehl, J.L.; Khare, S.V. Structural, Energetic and Elastic Properties of $Cu_2ZnSn(S_xSe_{1-x})_4$ (x = 1, 0.75, 0.5, 0.25, 0) Alloys from First-Principles Computations. *Sol. Energy* **2014**, *102*, 276–281. [CrossRef]
13. Simya, O.K.; Mahaboobbatcha, A.; Balachander, K. A Comparative Study on the Performance of Kesterite Based Thin Film Solar Cells Using SCAPS Simulation Program. *Superlattices Microstruct.* **2015**, *82*, 248–261. [CrossRef]
14. Atwater, H.A.; Polman, A. Plasmonics for Improved Photovoltaic Devices. *Nat. Mater* **2010**, *9*, 205–213. [CrossRef] [PubMed]
15. Green, M.; Dunlop, E.; Hohl-Ebinger, J.; Yoshita, M.; Kopidakis, N.; Hao, X. Solar Cell Efficiency Tables (Version 57). *Prog. Photovolt. Res. Appl.* **2021**, *29*, 3–15. [CrossRef]
16. Green, M.A.; Emery, K.; Hishikawa, Y.; Warta, W. Solar Cell Efficiency Tables (Version 37). *Prog. Photovolt. Res. Appl.* **2011**, *19*, 84–92. [CrossRef]
17. Kayes, B.M.; Nie, H.; Twist, R.; Spruytte, S.G.; Reinhardt, F.; Kizilyalli, I.C.; Higashi, G.S. 27.6% Conversion Efficiency, a New Record for Single-Junction Solar Cells under 1 Sun Illumination. In Proceedings of the 2011 37th IEEE Photovoltaic Specialists Conference, Seattle, WA, USA, 19–24 June 2011; pp. 000004–000008.
18. Green, M.A.; Emery, K.; Hishikawa, Y.; Warta, W.; Dunlop, E.D. Solar Cell Efficiency Tables (Version 43). *Prog. Photovolt. Res. Appl.* **2014**, *22*, 1–9. [CrossRef]
19. Mitzi, D.B.; Yuan, M.; Liu, W.; Kellock, A.J.; Chey, S.J.; Deline, V.; Schrott, A.G. A High-Efficiency Solution-Deposited Thin-Film Photovoltaic Device. *Adv. Mater.* **2008**, *20*, 3657–3662. [CrossRef]
20. Fthenakis, V.M.; Moskowitz, P.D. Photovoltaics: Environmental, Health and Safety Issues and Perspectives. *Prog. Photovolt. Res. Appl.* **2000**, *8*, 27–38. [CrossRef]
21. Tanaka, A. Toxicity of Indium Arsenide, Gallium Arsenide, and Aluminium Gallium Arsenide. *Toxicol. Appl. Pharmacol.* **2004**, *198*, 405–411. [CrossRef]
22. Phipps, G.; Mikolajczak, C.; Guckes, T. Indium and Gallium: Long-Term Supply. *Renew. Energy Focus* **2008**, *9*, 56–59. [CrossRef]
23. Patel, M.; Ray, A. Enhancement of Output Performance of Cu_2ZnSnS_4 Thin Film Solar Cells—A Numerical Simulation Approach and Comparison to Experiments. *Phys. B Condens. Matter* **2012**, *407*, 4391–4397. [CrossRef]
24. Nitsche, R.; Sargent, D.F.; Wild, P. Crystal Growth of Quaternary 122464 Chalcogenides by Iodine Vapor Transport. *J. Cryst. Growth* **1967**, *1*, 52–53. [CrossRef]
25. Lahoual, M.; Bourennane, M.; Aidaoui, L. Numerical Investigation of Copper Zinc Tin Sulphide Based Solar Cell with Non-Toxic Zn (O, S) Buffer Layer. *Phys. Status Solidi* **2024**, *221*, 2300732. [CrossRef]
26. Mansouri, S.; Dehimi, L.; Bencherif, H.; Pezzimenti, F.; Zulfiqar, M.; Alotaibi, N.H.; Mohammad, S.; Haldhar, R.; Darwish, M.A.; Hossain, M.K. Theoretical Simulation on Enhancing the Thin-Film Copper Zinc Tin Sulfide Solar Cell Performance Using MoS_2, MoOx, and CuI as Efficient Hole Transport Layers. *Energy Fuels* **2024**, *38*, 8187–8198. [CrossRef]
27. Dakua, P.K.; Dash, R.K.; Laidouci, A.; Bhattarai, S.; Dudekula, U.; Kashyap, S.; Agarwal, V.; Rashed, A.N.Z. Evaluating CZTS Solar Cell Performance Based on Generation and Recombination Models for Possible ETLs Through Numerical Analysis. *J. Electron. Mater.* **2024**, *53*, 2015–2025. [CrossRef]
28. Sawa, H.B.; Babucci, M.; Keller, J.; Björkman, C.P.; Samiji, M.E.; Mlyuka, N.R. Toward Improving the Performance of Cu_2ZnSnS_4-Based Solar Cells with Zr, W or Sulfurized Layers at the SnO_2:F/Cu_2ZnSnS_4 Rear Interface. *Thin Solid Film.* **2024**, *793*, 140276. [CrossRef]
29. Kissin, S.A.; Owens, D.A.R. The Relatives of Stannite in the Light of New Data. *Can. Mineral.* **1989**, *27*, 673–688.
30. Nakazawa, K.I. Electrical and Optical Properties of Stannite-Type Quaternary Semiconductor Thin Films. *Jpn. J. Appl. Phys.* **1988**, *27*, 2094. [CrossRef]
31. Cherouana, A.; Labbani, R. Study of CZTS and CZTSSe Solar Cells for Buffer Layers Selection. *Appl. Surf. Sci.* **2017**, *424*, 251–255. [CrossRef]

32. Niki, S.; Contreras, M.; Repins, I.; Powalla, M.; Kushiya, K.; Ishizuka, S.; Matsubara, K. CIGS Absorbers and Processes. *Prog. Photovolt. Res. Appl.* **2010**, *18*, 453–466. [CrossRef]
33. Amin, N.; Hossain, M.I.; Chelvanathan, P.; Mukter Uzzaman, A.S.M.; Sopian, K. Prospects of Cu2ZnSnS4 (CZTS) Solar Cells from Numerical Analysis. In Proceedings of the International Conference on Electrical & Computer Engineering (ICECE 2010), Dhaka, Bangladesh, 18–20 December 2010; pp. 730–733.
34. Shin, B.; Gunawan, O.; Zhu, Y.; Bojarczuk, N.A.; Chey, S.J.; Guha, S. Thin Film Solar Cell with 8.4% Power Conversion Efficiency Using an Earth-Abundant Cu_2ZnSnS_4 Absorber. *Prog. Photovolt. Res. Appl.* **2013**, *21*, 72–76. [CrossRef]
35. Adewoyin, A.D.; Olopade, M.A.; Chendo, M. Enhancement of the Conversion Efficiency of Cu_2ZnSnS_4 Thin Film Solar Cell through the Optimization of Some Device Parameters. *Optik* **2017**, *133*, 122–131. [CrossRef]
36. Siebentritt, S. Why Are Kesterite Solar Cells Not 20% Efficient? *Thin Solid Film.* **2013**, *535*, 1–4. [CrossRef]
37. Zanatta, A.R. The *Shockley–Queisser* Limit and the Conversion Efficiency of Silicon-Based Solar Cells. *Results Opt.* **2022**, *9*, 100320. [CrossRef]
38. Shockley, W.; Queisser, H. Detailed Balance Limit of Efficiency of p–n Junction Solar Cells. In *Renewable Energy*; Routledge: London, UK, 2011; ISBN 978-1-315-79324-5.
39. Lv, Z.; Deng, Z.; Xu, D.; Li, X.; Jia, Y. Efficient Organic Light-Emitting Diodes with C60 Buffer Layer. *Displays* **2009**, *30*, 23–26. [CrossRef]
40. Ferhati, H.; Djeffal, F.; AbdelMalek, F. Towards Improved Efficiency of SnS Solar Cells Using Back Grooves and Strained-SnO_2 Buffer Layer: FDTD and DFT Calculations. *J. Phys. Chem. Solids* **2023**, *178*, 111353. [CrossRef]
41. Isha, A.; Kowsar, A.; Kuddus, A.; Hossain, M.K.; Ali, M.H.; Haque, M.D.; Rahman, M.F. High Efficiency Cu_2MnSnS_4 Thin Film Solar Cells with SnS BSF and CdS ETL Layers: A Numerical Simulation. *Heliyon* **2023**, *9*, e15716. [CrossRef]
42. Gohri, S.; Sharma, S.; Pandey, R.; Madan, J.; Sharma, R. Influence of SnS and Sn_2S_3 Based BSF Layers on the Performance of CZTSSe Solar Cell. In Proceedings of the 2020 47th IEEE Photovoltaic Specialists Conference (PVSC), Calgary, AB, Canada, 15 June–21 August 2020; pp. 2300–2303.
43. Srivastava, A.; Dua, P.; Lenka, T.R.; Tripathy, S.K. Numerical Simulations on CZTS/CZTSe Based Solar Cell with ZnSe as an Alternative Buffer Layer Using SCAPS-1D. *Mater. Today Proc.* **2021**, *43*, 3735–3739. [CrossRef]
44. Burgelman, M.; Nollet, P.; Degrave, S. Modelling Polycrystalline Semiconductor Solar Cells. *Thin Solid Film.* **2000**, *361–362*, 527–532. [CrossRef]
45. Oublal, E.; Ait Abdelkadir, A.; Sahal, M. High Performance of a New Solar Cell Based on Carbon Nanotubes with CBTS Compound as BSF Using SCAPS-1D Software. *J. Nanopart. Res.* **2022**, *24*, 202. [CrossRef]
46. Rahman, M.A. Design and Simulation of a High-Performance Cd-Free Cu_2SnSe_3 Solar Cells with SnS Electron-Blocking Hole Transport Layer and TiO_2 Electron Transport Layer by SCAPS-1D. *SN Appl. Sci.* **2021**, *3*, 253. [CrossRef]
47. Mohandes, A.; Moradi, M.; Kanani, M. Numerical Analysis of High Performance Perovskite Solar Cells with Stacked ETLs/C60 Using SCAPS-1D Device Simulator. *Opt. Quant. Electron.* **2023**, *55*, 533. [CrossRef]
48. Atowar Rahman, M. Enhancing the Photovoltaic Performance of Cd-Free Cu_2ZnSnS_4 Heterojunction Solar Cells Using SnS HTL and TiO_2 ETL. *Sol. Energy* **2021**, *215*, 64–76. [CrossRef]
49. Islam, M.A.; Al Rafi, J.; Uddin, M.A. Modeling and Formation of a Single-Walled Carbon Nanotube (SWCNT) Based Heterostructure for Efficient Solar Energy: Performance and Defect Analysis by Numerical Simulation. *AIP Adv.* **2023**, *13*, 115201. [CrossRef]
50. Uddin, M.A.; Rafi, J.A.; Islam, M.A.; Mominuzzaman, S.M.; Nath, I.D. Modeling and Numerical Analysis of Heterostructure Single-Walled Carbon Nanotube (SWCNT) Solar Cell. In Proceedings of the 2022 12th International Conference on Electrical and Computer Engineering (ICECE), Dhaka, Bangladesh, 21–23 December 2022; pp. 388–391.